Chemical Engineering Science 267 (2023) 118336

Contents lists available at ScienceDirect

Chemical Engineering Science

journal homepage: www.elsevier.com/locate/ces

Modeling the reactive flow of semi-continuous mixtures by the adaptive characterization method

Daniele C. Rocha [a,b], Paulo L.C. Lage [a,*]

[a] Programa de Engenharia Química — COPPE, Universidade Federal do Rio de Janeiro, PO Box 68502, 21941-972 Rio de Janeiro, RJ, Brazil
[b] Petrobras – Edifício Senado (EDISEN), Av. Henrique Valadares 28, 20231-030 Rio de Janeiro, RJ, Brazil

HIGHLIGHTS

- Reactive flows of semi-continuous mixtures were solved for hydrocarbon hydrocracking.
- We extended the adaptive characterization method using (DQMoM) to reactive flows.
- We also extended the fixed point quadrature method (FPQM) to flow problems.
- DQMoM gave more accurate solutions than FPQM for the test cases.
- DQMoM was 4.9 times faster than FPQM for the reactive flow test case.

ARTICLE INFO

Article history:
Received 26 September 2022
Received in revised form 13 November 2022
Accepted 20 November 2022
Available online 25 November 2022

Keywords:
Reactive flows
CFD
DQMoM
Continuous lumping
Quadrature-based moment methods
OpenFOAM

ABSTRACT

This work proposes and analyzes the direct quadrature method of moments (DQMoM) applied to the adaptive characterization of pseudo-components for simulating semi-continuous reactive mixtures' flow. We also extended the fixed point quadrature method (FPQM) by expanding its scope to solve field problems and use discrete distributions as initial or inlet data. We implemented both methods in OpenFOAM® and used them to simulate the thermal cracking of hydrocarbon mixtures, guaranteeing mesh convergence. The FPQM results showed poor convergence behavior, while the DQMoM results converged regarding the number of quadrature points. DQMOM was up to 4.9 faster than FPQM for our reactive flow test case.

1. Introduction

The proper design, control, and evaluation of the refinery conversion and treatment units require accurate modeling of the process streams, motivating oil companies to develop new technologies to optimize and simulate the flow of petroleum fractions. In this context, computational fluid dynamics (CFD) is a powerful tool to investigate and predict the phenomenological behavior of the fluids and the transport phenomena that occur during the flow of these streams.

The oil streams are multicomponent mixtures composed of hundreds of species undergoing reactions, which makes it not practical or even possible to identify all species, much less simulate their behavior using detailed kinetic mechanisms in CFD.

Thus, these mixtures' thermodynamic and kinetic modeling often starts by applying an order reduction method, whose types are reviewed by Okino and Mavrovouniotis (1998). Here we focused on the continuous lumping approach, where the composition of the many-component mixture is represented by a distribution function of a convenient variable, which can be a chemical (Laxminarasimhan et al., 1996) or physical property (Lage, 2007; Rocha and Lage, 2020) or even a non-physical mathematical variable (Singer et al., 2021).

Laxminarasimhan et al. (1996) developed the fixed point quadrature method (FPQM), which defines a partition of the distribution variable domain into classes and approximates the concentration continuous distribution by linear functions in each class. This approach was applied to the zeroth-dimensional modeling of the temporal variations of concentration caused by hydrocracking reactions (Elizalde et al., 2009; Rocha and Lage, 2020). It was extended to field problems for the first time by Vergel et al. (2015), which implemented the FPQM algorithm in the commer-

* Corresponding author.
E-mail addresses: drocha@petrobras.com.br (D.C. Rocha), paulo@peq.coppe.ufrj.br (P.L.C. Lage).

https://doi.org/10.1016/j.ces.2022.118336
0009-2509/

Nomenclature

a_i	source term in Eq. (8)
b_f	fragmentation specific frequency
b_i	source term in Eq. (9)
$B_{i,k}$	matrix defined by Eq. 21
C	molar concentration
c_i	defined in Eq. (11)
D	effective diffusion coefficient
d	number of discrete components in the semi-continuous mixture
e_i	defined in Eq. (13)
F	cumulative distribution
f	mass concentration distribution function
f_C	molar concentration distribution function
g_i	defined in Eq. (16)
G_i	defined in Eq. (18)
h_i	defined in Eq. (16)
H_i	defined in Eq. (18)
I	distribution variable, quadrature abscissa ou node
$\mathbf{I}$	identity matrix
J	pseudo-component in initial or inlet discrete distribution
ℓ	Legendre polynomial
L	defined in Eq. 14
M	molar mass
m	number of discrete pseudo-components in each partition interval
M_n	number-average molar mass
M_w	mass-average molar mass
N	number of quadrature points (discretized pseudo-components)
n	number of intervals in FPQM
p	pressure
$\mathscr{P}_n$	n-interval partition of the distribution variable domain
q	number of pseudo-components in initial or inlet discrete distribution
r	rate of reaction
R	universal gas constant
s	number of terms in the Fourier series expansion
$\mathbf{S}$	normal surface area vector
t	time
T	temperature
u_i	defined in Eq. (12)
$\mathbf{v}$	velocity
w_j	weight of the discrete component j
$\mathbf{x}$	spatial position vector
y	y-coordinate

Greek letters

δ	Dirac delta function
ε	tolerance
γ	average uncertainty
κ	iteration
λ	regular moment
μ	viscosity
ν	yield function upon fragmentation
ξ	integral terms defined in Eqs. (22)–(24)
ρ	density or mass concentration
$\tilde{\rho}$	pseudo-component mass concentration in initial or inlet discrete distribution
σ	constant kinetic rate of fragmentation
ϕ	mass flow rate
ϕ^c	area flow rate caused by the mixture compressibility
ϕ^v	volume flow rate
Φ	Fourier coefficient
φ	generic variable
ψ	density-pressure linear factor
ω	quadrature weight
Ω	probability density distribution for the fragmentation

Subscripts

abs	absolute
C	molar concentration
f	interpolated to face volume
j	discrete component index
max	maximum value
min	minimum value
ref	reference
rel	relative
w	mass

Abbreviations

CFD	computational fluid dynamics
DQMoM	direct quadrature method of moments
FPQM	fixed point quadrature method
GCI	Grid convergence index
HGO	Heavy gas oil
LGO	light gas oil
LPG	Liquefied petroleum gas
NVD	normalized variable diagram
QBMM	quadrature-based moment methods
TVD	total variation diminishing

cial CFD code ANSYS CFX to simulate the yield curve of a fluid catalytic cracking unit. They highlighted that selectivity and conversion are affected by the hydrodynamic effects.

Lage (2007) proposed the application of quadrature-based methods of moments (QBMM), originally developed for the solution of population balance problems (McGraw, 1997; Marchisio and Fox, 2005), for the adaptive characterization of the molar fraction distribution of a continuous component in a complex mixture. Lage (2007) applied it to flash and flow mixing calculations involving hydrocarbon mixtures. Afterwards, Laurent et al. (2009) and Singer (2016) applied QBMMs to multicomponent droplet vaporization, Rodrigues et al. (2012) and Chicralla et al. (2019) to multistage separation of continuous multicomponent mixtures, and Petitfrere et al. (2014) to two and three-phase flash calculations of petroleums. Recently, Singer et al. (2021) modified the multicomponent droplet vaporization model developed by Cooney and Singer (2018) that uses DQMoM (direct quadrature method of moments). They define a non-physical distribution variable that allows modeling the reactive gas species' evaporation fluxes.

Jatobá (2010) was the first to apply the adaptive characterization method using DQMoM to simulate incompressible flows of continuous mixtures using OpenFOAM® (Weller et al., 1998). This work was later extended by the same author (Jatobá et al., 2014) for compressible flows, showing that the QBMM, or more specifically the DQMoM, can accurately calculate the flow of a non-reactive continuous mixture with reduced computational time.

Rocha and Lage (2020) applied the direct quadrature method of generalized moments (DQMoGeM) (Santos et al., 2013) to the evolution of reactive hydrocarbon mixtures, leading to accurate solutions with small numbers of quadrature points. These methods

are adequate for implementation in CFD codes since a small number of points allows for faster simulations. For thermal craking, they also obtained the solution using the fixed point quadrature method (FPQM), employed previously by Elizalde et al. (2009).

In this work, the DQMoM was employed for the first time to model the flow of semi-continuous mixtures with mass transfer due to diffusion, advection, and chemical reactions. Therefore, it is an extension of both Jatobá et al. (2014) and Rocha and Lage (2020) works. For comparison purposes, we also extended the FPQM, as implemented by Rocha and Lage (2020), to reactive flow problems of semi-continuous mixtures. Both methods were implemented in OpenFOAM®.

2. Mathematical model

Following Jatobá et al. (2014), we describe the mathematical model for the reactive isothermal flow of a compressible gaseous semi-continuous mixture subject to thermal cracking composed by the equations of motion and the mass conservation equations. The equations of motions are the continuity equation, given by

$$\frac{\partial \rho}{\partial t} + \nabla \cdot (\rho \mathbf{v}) = 0 \tag{1}$$

and the momentum conservation equation for a Newtonian fluid, given by:

$$\begin{aligned}\frac{\partial (\rho \mathbf{v})}{\partial t} + \nabla \cdot (\rho \mathbf{v}\mathbf{v}) - \nabla \cdot \left\{ \mu \left[(\nabla \mathbf{v})^T - \frac{2}{3} (\nabla \cdot \mathbf{v}) \mathbf{I} \right] \right\} \\ - \nabla \cdot (\mu \nabla \mathbf{v}) = -\nabla p\end{aligned} \tag{2}$$

where the superscript T indicates tensor transposition.

The mixture composition model consists of one continuous component and some discrete components. The latter are non-reactant, and their mass conservation equations are given by:

$$\frac{\partial \rho_j}{\partial t} + \nabla \cdot \left(\rho_j \mathbf{v} \right) = \nabla \cdot \left[D_j \left(\nabla \rho_j - \rho_j \frac{\nabla \rho}{\rho} \right) \right] \tag{3}$$

where the term on the right-hand side is the negative of the divergence of the Fickian diffusive flux, given by $-\rho D_j \nabla (\rho_i / \rho)$.

For the reactive continuous component, the mass conservation equations in terms of the mass concentration distribution, $f(I)$, is given by:

$$\frac{\partial f(I)}{\partial t} + \nabla \cdot (f(I) \mathbf{v}) = \nabla \cdot \left[D(I) \left(\nabla f(I) - f(I) \frac{\nabla \rho}{\rho} \right) \right] + r(I) \tag{4}$$

where only the dependence on the distribution variable I is explicitly given. Note that I is any property of the continuous component that we can assume to be the distribution variable for the mass concentration of the continuous component. Therefore, I can be any monotonic continuous function of the molar mass, boiling point, specific reaction rate, etc.

For thermal cracking, the model for $r(I)$ comes from the population balance modeling of fragmentation for a univariate distribution, given by (Rocha and Lage, 2020):

$$r(I) = -b_f(I) f(I) + \int_I^\infty v(I\prime) b_f(I\prime) \Omega(I, I\prime) f(I\prime) dI\prime \tag{5}$$

The solution of this model requires the discretization of the continuous component in pseudo-components and the definition of the kinetic reaction model. The latter requires the definition of b_f, v and Ω for the thermal cracking process (Elizalde et al., 2009). The former is summarized in the following sections and detailed in the previous works (Jatobá et al., 2014; Rocha and Lage, 2020). When r is the mass source per unit volume due to reaction, as in Eq. (5) and the sum of the masses of all fragments is equal to the mass of the fragmenting component, then $v = 1$. We assumed $v = 1$ in the present work.

3. Numerical solution of reactive flows of continuous mixtures

In the following, we describe the usage of the adaptive characterization method for the reactive flow of semi-continuous mixtures, which consists of the DQMOM application to Eq. (4). We also present an extension of the FPQM to flow problems.

3.1. DQMoM solution of the reactive flow

The application of DQMoM basically consists of replacing the distribution function in Eq. (4) by its discrete approximation:

$$f(I, t, \mathbf{x}) = \sum_{i=1}^{N} \omega_i(t, \mathbf{x}) \delta(I - I_i(t, \mathbf{x})) \tag{6}$$

where I_i and ω_i are the abscissas and weights of the Gauss-Christoffel quadrature computed using the first $2N$ moments of f, followed by the application of the moment operator:

$$\int_{I_{min}}^{I_{max}} I^k \cdot dI, \quad k = 0, \ldots, \infty \tag{7}$$

where $[I_{min}, I_{max}] \supseteq \sup f$. This procedure, given in detail in the Appendix A, generates the conservation equations for the weights (mass concentrations) and abscissas (values of the distribution variable) that characterize the adaptive pseudo-components, given by:

$$\frac{\partial \omega_i}{\partial t} + \nabla \cdot (\omega_i \mathbf{v}) - \nabla \cdot (D(I_i) \nabla \omega_i) + \nabla \cdot \left(\omega_i D(I_i) \frac{\nabla \rho}{\rho} \right) = a_i \tag{8}$$

$$\begin{aligned}\frac{\partial I_i}{\partial t} + \nabla \cdot (I_i \mathbf{v}) - I_i (\nabla \cdot \mathbf{v}) - \nabla \cdot (D(I_i) \nabla I_i) + \nabla \cdot \left(I_i D(I_i) \frac{\nabla \rho}{\rho} \right) \\ - \nabla \cdot \left(D(I_i) \frac{\nabla \rho}{\rho} \right) I_i = b_i\end{aligned} \tag{9}$$

The source terms a_i and b_i are determined by the solution of the following linear system:

$$\begin{aligned}\sum_{i=1}^{N} I_i^k a_i \quad + \sum_{i=1}^{N} \omega_i k I_i^{k-1} b_i = \sum_{i=1}^{N} u_i k I_i^{k-1} + \sum_{i=1}^{N} e_i I_i^k \\ + \sum_{i=1}^{N} \omega_i b_f(I_i) \left(v(I_i) L_k(I_i) - I_i^k \right) \\ + \sum_{i=1}^{N} c_i \left(k(k-1) I_i^{k-2} D(I_i) + 2k I_i^{k-1} D\prime(I_i) + I_i^k D\prime\prime(I_i) \right)\end{aligned} \tag{10}$$

where

$$c_i = \omega_i \nabla I_i \cdot \nabla I_i \tag{11}$$

$$u_i = 2 D(I_i) \nabla \omega_i \cdot \nabla I_i \tag{12}$$

$$e_i = 2 D\prime(I_i) \nabla \omega_i \cdot \nabla I_i + \nabla \cdot (D\prime(I_i) \nabla I_i) \omega_i - \omega_i D\prime(I_i) \frac{\nabla \rho}{\rho} \cdot \nabla I_i \tag{13}$$

and $L_k(I)$ is defined

$$L_k(I) = \int_{I_{min}}^{I} I^k \Omega(I\prime, I) dI\prime \tag{14}$$

3.2. FPQM solution of the reactive flow

The FPQM approximates the f distribution using piecewise linear functions between $(n+1)$ fixed discretization points (nodes), I_i:

$$f(I) = g_i(I)f(I_i) + h_i(I)f(I_{i+1}), \quad I \in [I_i, I_{i+1}], \quad i = 0, \ldots, n-1 \tag{15}$$

where

$$g_i(I) = \frac{I_{i+1} - I}{I_{i+1} - I_i}, \qquad h_i(I) = \frac{I - I_i}{I_{i+1} - I_i} \tag{16}$$

for any n-interval partition, $\mathscr{P}_n = \{I_0, I_1, \ldots, I_n\}$, of the distribution variable domain. The FPQM initialization needs the $(n+1)$ nodal values of $f(I_i)$ at $t = 0$ (Laxminarasimhan et al., 1996).

The nodal values of the distribution are related to the zeroth-order sectional moments of the continuous concentration distribution, ρ_i, by:

$$\rho_i(t) = \int_{I_i}^{I_{i+1}} f(I,t)\,dI = G_i f(I_i,t) + H_i f(I_{i+1},t), \quad i = 0, \ldots, n-1, \tag{17}$$

where

$$G_i = \int_{I_i}^{I_{i+1}} g_i(I)dI, \quad H_i = \int_{I_i}^{I_{i+1}} h_i(I)dI, \tag{18}$$

The ρ_i value is the mass concentration of the pseudo-component that represent all components in the $[I_i, I_{i+1}]$ interval.

Elizalde et al. (2009) used the approach proposed by Govindhakannan and Riggs (2007) to calculate the $(n+1)$ nodal values, $f(I_i, 0)$, from the n values of $\rho_i(0)$, which can be computed from the initial concentration distribution. Since there are more unknowns than variables, Govindhakannan and Riggs (2007) proposed minimizing the sum of the squares of the differences between consecutive $f(I_i, 0)$ values to close the problem. Accordingly to Elizalde et al. (2009), the error in the numerical discretization of the continuous initial concentration distribution decreases by increasing the value of n.

In the present work, we use initial discrete concentration distributions, and therefore, we developed a different methodology for the FPQM initialization. Let us consider an initial discrete mass concentration distribution given by:

$$f(I,0) = \sum_{j=1}^{q} \tilde{\rho}_j \delta(I - J_j) \tag{19}$$

where $\tilde{\rho}_j$ is the initial mass concentration of the pseudo-component represented by J_j.

The cornerstone of the proposed methodology is to include an integer number of such pseudo-components, m, within each interval $[I_i, I_{i+1}]$ of the partition $\mathscr{P}_n$. This is easily done for $m = 1$ by making $n = q$ and defining the partition nodes in a way that they satisfy $J_i \in (I_{i-1}, I_i), i = 1, \ldots, n$. In order to estimate the discretization error, we also considered the cases with $m = 2$ and 3. Appendix B gives the details.

The FPQM consists in applying Eqs. (4) and (5) at the nodes, I_i, using the piecewise linear approximation of the concentration distribution, given by Eq. (15), to substitute $f(I\prime)$ in the integral term. By the procedure described by Elizalde et al. (2009), we arrived at the following conservation equations for the nodal point values:

$$\frac{\partial f(I_i,t)}{\partial t} + \nabla\cdot(f(I_i,t)\mathbf{v}) - \nabla\cdot\left[D(I_i)\left(\nabla f(I_i,t) - f(I_i,t)\frac{\nabla\rho}{\rho}\right)\right] = \sum_{k=0}^{n} f(I_k,t)B_{i,k}, \tag{20}$$

where

$$[B_{i,k}] = \begin{bmatrix} -b_f(I_0)+\xi_{1,0} & \xi_{2,1}+\xi_{3,1} & \cdots & \xi_{2,j}+\xi_{3,j} & \cdots & \xi_{2,n} \\ 0 & -b_f(I_1)+\xi_{1,1} & \cdots & \xi_{2,j}+\xi_{3,j} & \cdots & \xi_{2,n} \\ 0 & 0 & \ddots & \vdots & \cdots & \vdots \\ \vdots & \vdots & \vdots & b_f(I_i)+\xi_{1,i} & \cdots & \vdots \\ \vdots & \vdots & \vdots & \vdots & \ddots & \vdots \\ 0 & 0 & \cdots & 0 & \cdots & -b_f(I_n) \end{bmatrix} \tag{21}$$

and

$$\xi_{1,i} = \int_{I_i}^{I_{i+1}} v(I\prime)\Omega(I_i,I\prime)b_f(I\prime)g_i(I\prime)dI\prime \tag{22}$$

$$\xi_{2,j} = \int_{I_{j-1}}^{I_j} v(I\prime)\Omega(I_i,I\prime)b_f(I\prime)h_{j-1}(I\prime)dI\prime \tag{23}$$

$$\xi_{3,j} = \int_{I_j}^{I_{j+1}} v(I\prime)\Omega(I_i,I\prime)b_f(I\prime)g_j(I\prime)dI\prime \tag{24}$$

4. Numerical procedure

The discretization and solution algorithm for the governing equations presented in Section 2 were implemented in OpenFOAM®-4.x. We employed the C#, C, and FORTRAN languages to write auxiliary routines for pre and post-processing data.

All computations were performed using double precision arithmetics (16 significant digits) and four CPU cores of a cluster node with Intel Xeon Gold 6248 processors at 2.5 GHz and 384 Gb of RAM.

4.1. Implementation of the code

Because this work is an extension for reactive flows of the modeling developed by Jatobá et al. (2014), we rely on their description of most of the code implementation. They showed the details of the discretization procedure applied to the differential operators of the continuity, momentum, and species equations, besides the pressure–velocity correction algorithm.

In this work, we modified the DCM and DQMOM OpenFOAM® codes developed by Jatobá et al. (2014) and added the FQPM and DQMoM reaction terms. In both codes, we implemented the reaction terms as time-explicit source terms. For the FPQM, Eq. (20) can be written as:

$$\left\lfloor\frac{\partial[f(I_i,t)]}{\partial t}\right\rfloor + \lfloor\nabla\cdot(\phi^v[f(I_i,t)])\rfloor + \lfloor\nabla\cdot(D(I_i)\phi^c[f(I_i,t)])\rfloor - \lfloor\nabla\cdot(D(I_i)\nabla[f(I_i,t)])\rfloor = \sum_{k=0}^{n} B_{i,k}f(I_k,t) \tag{25}$$

where $\lfloor\cdot\rfloor$ represents an implicit discretization in time, the lack of it implies an explicit scheme. Moreover, $[\cdot]$ denotes the variable solved by the discretized equation. The reaction term can be easily determined, since it is computed from the current values of $f(I_k,t)$ and the $B_{i,k}$ matrix, which involves the computation of the integrals given by Eqs. (22)–(24) (Elizalde et al., 2009).

For the DQMoM code, Eqs. (8) and (9) for the transport equations for the weights and abscissas are written as:

$$\left\lfloor\frac{\partial[\omega_i]}{\partial t}\right\rfloor + \lfloor\nabla\cdot(\phi^v[\omega_i])\rfloor - \lfloor\nabla\cdot(D(I_i)\nabla[\omega_i])\rfloor + \lfloor\nabla\cdot(D(I_i)\phi^c[\omega_i])\rfloor = a_i \tag{26}$$

$$\left\lfloor\frac{\partial[I_i]}{\partial t}\right\rfloor + \lfloor\nabla\cdot(\phi^v[I_i])\rfloor - \lfloor\nabla\cdot(\phi^v)[I_i]\rfloor - \lfloor\nabla\cdot(D(I_i)\nabla[I_i])\rfloor + \lfloor\nabla\cdot(D(I_i)\phi^c[I_i])\rfloor - \lfloor\nabla\cdot(D(I_i)\phi^c)[I_i]\rfloor = b_i \quad (27)$$

where a_i and b_i were calculated by solving the linear system given by Eq. (10) using the current values of ω_i and I_i, ϕ^v and ϕ^c represent volume and area flow rates across control volume faces by convection and by mixture compressibility, respectively, being defined as $\phi^v = \mathbf{S}\cdot(\mathbf{v})_f$ and $\phi^c = \mathbf{S}\cdot(\nabla\rho/\rho)_f$, where $\mathbf{S}$ is the face area vector of a control volume and the subscript f indicates values interpolated to this face.

Although the solvers developed by Jatobá et al. (2014) are the basis of our implementation for the reactive flow simulation, we had to carry out some structural modifications to guarantee the solution convergence because the inclusion of the reaction term transforms the formulation into a stiff system of differential equations. It is important to emphasize that these modifications were essential for the FPQM code to achieve stability. We listed the main changes below.

1. In the DQMoM solution, we replaced the formulation based on the solution of the transport equations for the weights and weighted-abscissa, $\omega_i I_i$, with the formulation that solves the equations for the weights and abscissas since (Santos et al., 2013) proved that it is more robust than the former.
2. In the convergence loop, we included an additional criterion for the velocity components, according to the mixed tolerance criteria defined by:

$$\max\left[\frac{|\varphi^\kappa - \varphi^{\kappa-1}|}{\varepsilon_{abs} + \varepsilon_{rel}|\varphi^\kappa|}\right] < 1.0$$

where φ represents the velocity components.
3. We updated the pressure–velocity coupling algorithm to PIMPLE, which is best than PISO, used by Jatobá et al. (2014) in the OpenFOAM® version 1.6-ext.

The DQMoM and FPQM formulations were implemented in two different solvers, named as *mrtDqmomFoam* and *mrtFoam*, respectively. The former was developed from the *mmtDqmomFoam* and the latter from the *mmtFoam*, both built by Jatobá et al. (2014). The algorithm for each time step in the *mrtDqmomFoam* solver can be summarized as follows.

1. Prediction of the evolution of the mixture density, using the discretized form of Eq. (1).
2. Velocity prediction based on the discretized form of the Eq. (2).
3. Solution of the transport equations for the weights and abscissas, Eqs. (26) and (27).
4. Solution of the discretized form of the species conservation equation for the discrete components (Eq. 3).
5. Mixture density estimation, stored as ρ^* and calculated by:

$$\rho = \sum_{j=1}^{d}\rho_j + \sum_{i=1}^{N}\rho_i \quad (29)$$

where $\rho_i = \omega_i$ since f is the mass concentration distribution of the continuous component.
6. Average molar mass calculation:

$$M_n = \left[\sum_{j=1}^{d}\frac{\rho_j}{\rho^* M_j} + \sum_{i=1}^{N}\frac{\rho_i}{\rho^* M_i}\right]^{-1} \quad (30)$$

7. Density-pressure linear factor, ψ, calculation using:

$$\psi = \frac{M_n}{RT} \quad (31)$$

8. Mixture density calculation, stored as ρ and calculated by:

$$\rho = \psi(p + p_{ref}) \quad (32)$$

9. Correction of ρ_j and ω_i by multiplying them by (ρ/ρ^*).
10. If the convergence of Eq. (28) is achieved for ω_i and I_i or the number of iteration steps exceeds the maximum number set for the mass loop, go to step 11, otherwise, go to step 3.
11. Apply the velocity and pressure field corrections by using the PIMPLE algorithm until Eq. (28) converges or the number of iteration steps exceeds the maximum number set for the pressure loop.
12. If the convergence of Eq. (28) is achieved or the number of iteration steps exceeds the maximum number set for the velocity loop, go to step 13, otherwise, go to step 2.
13. Mixture density calculation using Eq. (32).
14. Calculation of the first two moments of the semi-continuous mixture:

$$\lambda_k(t) = \sum_{j=1}^{d}\rho_j M_j^k + \sum_{i=1}^{N}\rho_i M_i^k, \quad k = 0, 1 \quad (33)$$

15. Mass average molar mass calculation:

$$M_w = \frac{\lambda_1}{\lambda_0} \quad (34)$$

The *mrtFoam* algorithm is similar to the steps described above. The differences are: the solution of Eq. (25) at step 3, instead of Eqs. (26) and (27), the inclusion of a new step between steps 4 and 5 to perform the mass concentration calculation through Eq. (17) and the replacement of the ω_i and I_i by $f(I_i, t)$ at steps 9 and 10.

4.2. Test cases description

The DQMOM and FPQM-based solvers were analyzed using two test cases. The first one aimed to verify the code implementation and the accuracy of the FPQM and DQMoM-based solvers (*mrtDqmomFoam and mrtFoam*) against the analytical solution using a zero-dimensional model. The other case is a modification of the one analyzed by Jatobá et al. (2014), whose aim is to compare the accuracy and performance of the two solvers for the reactive flow of a semi-continuous mixture. The description of both cases follows.

4.2.1. Test case 1

This test case consists of the evolution of the molar concentration distribution of a mixture consisting of a single continuous component due to thermal cracking in a batch reactor. The parameters chosen for the reaction rate allow an analytical solution for the distribution moments. According to Mccoy (1996), the fragmentation model is given by:

$$\frac{\partial f_C(I,t)}{\partial t} = -\sigma f_C(I,t) + 2\sigma\int_I^{I_{max}}\frac{1}{I\prime}f_C(I\prime,t)dI\prime \quad (35)$$

where $\sigma = 0.175$ is the constant kinetic rate, which is high enough to cause significant variations in the concentration distribution, and $I = M/M_{ref}$ is the distribution variable, being $M_{ref} = 0.398$, which is the maximum mixture molar mass at $t = 0$. Since cracking only reduces the molar mass, $f_C(I) = 0$ for $I > I_{max}$ and $\forall t$, and, therefore, $I_{max} = 1.0$. Due to the uniform distribution of the products, we must choose $I_{min} = 0$. Besides, as $f(I,t) = Mf_C(I,t)$, Eq. (35) can be rewritten as:

$$\frac{\partial f(I,t)}{\partial t} = -\sigma f(I,t) + 2\sigma \int_{I}^{I_{max}} \frac{1}{I\prime} \frac{I}{I\prime} f(I\prime,t) dI\prime \tag{36}$$

Mccoy (1996) gives the analytical solution of Eq. (35) in terms of the moments of f_C, which are related to the moments of f by:

$$\lambda_k(t) = \int_{I_{min}}^{I_{max}} I^k f(I,t) dI = M_{ref} \int_{I_{min}}^{I_{max}} I^{k+1} f_C(I,t) dI \tag{37}$$

The zeroth-order moment of f is the mass concentration of the mixture:

$$\lambda_0(t) = \int_{I_{min}}^{I_{max}} f(I,t) dI = \rho(t) \tag{38}$$

while the zeroth-order moment of f_C is the molar concentration of the mixture, which can be related to λ_{-1}:

$$C(t) = \int_{I_{min}}^{I_{max}} f_C(I,t) dI = \frac{1}{M_{ref}} \int_{I_{min}}^{I_{max}} I^{-1} f(I,t) dI = \frac{\lambda_{-1}(t)}{M_{ref}} \tag{39}$$

Thus, the number average molar mass of the mixture is calculated by:

$$M_n(t) = \frac{\lambda_0(t)}{\lambda_{-1}(t)} M_{ref} \tag{40}$$

while λ_1 can be used to compute the mass average molar mass:

$$M_w(t) = \frac{\lambda_1(t)}{\lambda_0(t)} M_{ref} \tag{41}$$

The DQMoM solution computes λ_0 and λ_1 directly from the quadrature weights and abscissas whereas the value of λ_{-1} comes from the quadrature approximation of the f integral in Eq. (39). Therefore, M_n is not as accurate as M_w.

As FPQM and DQMoM-based solvers quickly compute M_n and M_w, which are relevant response variables, we used their time evolution to analyze both methods by calculating their error concerning the analytical solution.

The initial gas mixture distribution consisted of 63 linear alkanes, corresponding to the continuous component distribution employed by Jatobá et al. (2014). To guarantee mass conservation, we included the alkanes with integer carbon numbers with molar masses less than 0.087 kg/mol as pseudo-components with zero mass fraction. Table 1 shows the mixture composition.

4.2.2. Test case 2 - Two-dimensional "T" channel

This test comes from Jatobá et al. (2014), which consists of mixing two streams in the two-dimensional "T" channel shown in Fig. 1. In this process, two gases with different compositions are fed at separate inlets and converge for a single output, promoting high concentration gradients, especially in the region near line A indicated in Fig. 1.

In Jatobá et al. (2014) work, the concentrations varied exclusively because of the mixing process. Here, the composition changes also occur due to thermal cracking reactions modeled by Eq. (36). As in Jatobá et al. (2014), the channel was initially filled with pure nitrogen at rest, at the pressure of 1 bar and temperature of 650 K. The discrete mass fraction distributions of the two gaseous streams fed to inlets 1 and 2 are the same used by Jatobá et al. (2014). As in the previous case, we included the alkanes with integer carbon numbers with molar masses less than 0.087 Kg/mol as pseudo-components but with zero mass fraction at the inlets. The process was isothermal. The gases followed the ideal gas law. They were fed at a speed of 0.1 m/s, resulting in a laminar flow with Reynolds of approximately 1700. At this speed, the flow reached the steady state at the outlet at approximately 5 s. The continuous components undergo cracking with the same kinetic rate ($\sigma = 0.175$) as soon as the gases enter the channel.

4.3. Solution Strategy

The discretization schemes adopted to solve the cases described in the previous section were similar to that used by Jatobá et al. (2014). Thus, the second order implicit scheme was adopted for the temporal term, the NVD gamma scheme (Gaskell and Lau, 1988; Leonard, 1988) for the convective term of momentum equation (Eq. 2) and the TVD limited linear scheme (Harten, 1983) for the convective terms of the mass transport equations (Eqs. 25–27).

Note that a single velocity field advects all mixture components, including the quadrature abscissas and weights representing the continuous component. Thus, there is no realizability loss of the corresponding moment set due to differences in the discretization of the advection fluxes of the abscissas and weights. However, the reader should be aware that improved numerical schemes are available (Vikas et al., 2011; Laurent and Nguyen, 2017) and the fully-conservative version of DQMOM (Buffo et al., 2013), which mitigates this problem, does exist.

Table 1
Initial mixture composition for test case 1.

M [kg/mol]	w_j(%)	M [kg/mol]	w_j(%)	M [kg/mol]	w_j(%)
0.001	0.0000	0.129	0.0695	0.228	4.5186
0.016	0.0000	0.132	0.0878	0.234	5.0119
0.030	0.0000	0.135	0.1063	0.241	5.6359
0.044	0.0000	0.139	0.1347	0.249	6.3071
0.058	0.0000	0.142	0.1678	0.256	6.9552
0.072	0.0000	0.146	0.2038	0.263	7.5192
0.087	0.0030	0.149	0.2557	0.270	7.8029
0.090	0.0027	0.153	0.3140	0.277	7.6005
0.092	0.0034	0.157	0.3807	0.284	6.8566
0.095	0.0041	0.160	0.4703	0.291	5.5807
0.097	0.0060	0.165	0.6629	0.299	4.0411
0.100	0.0062	0.170	0.8274	0.307	2.7441
0.103	0.0090	0.175	1.0480	0.316	1.7785
0.106	0.0113	0.181	1.2896	0.325	1.1524
0.108	0.0142	0.186	1.5817	0.334	0.7017
0.111	0.0175	0.192	1.8938	0.342	0.4039
0.114	0.0223	0.197	2.2000	0.352	0.2125
0.117	0.0266	0.202	2.5575	0.362	0.1118
0.120	0.0340	0.208	2.9903	0.371	0.0537
0.123	0.0430	0.214	3.4721	0.383	0.0335
0.126	0.0539	0.221	3.9955	0.398	0.0116

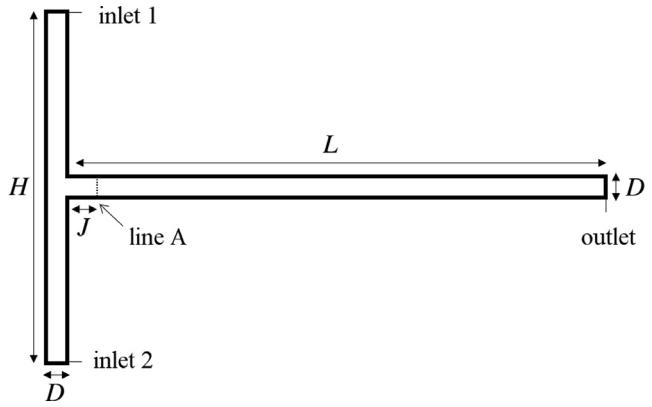

Fig. 1. "T" channel geometry used in test case 2 (L = 0.5 m; D = 0.01 m; H = 0.21 m; J = 0.01 m).

Due to the existence of cracking reactions and, therefore, the displacement of the distribution in the direction of the lighter compounds, it was necessary to use the multi-directional cell limiter to avoid overshoots for the gradient computations and hence negative values for the abscissas. To ensure stability for the gradient calculations, we kept the time step constant and equal to 10^{-5} s during all the simulations. As this is not a general solution for the problem of negative weights and abscissas, the reader should be aware that there are particular methods to deal with it. One is the time integration scheme that combines explicit methods of variable orders to preserve the realizability of the moment set (Nguyen et al., 2016), implemented in OpenQBMM (Passalacqua et al., 2018). Another is adding a stabilization term twice in the conservation equation with opposite signs, discretized both explicitly and implicitly, which increases the diagonal dominance of the discretization matrix, preventing the relevant variable from oscillating and reaching negative values (Favero et al., 2016).

The maximum number of iterations specified for the mass, pressure, and velocity loops was 20. The absolute and relative tolerances adopted for all variables were $\varepsilon_{abs} = 10^{-7}$ and $\varepsilon_{rel} = 10^{-6}$, respectively, except for the pressure that was $\varepsilon_{abs} = 10^{-5}$ and $\varepsilon_{rel} = 10^{-4}$, respectively.

4.4. Grid convergence analysis

We carried out the simulations of the second test case using different grids to ensure the independence of the results regarding spatial discretization. We employed the grid convergence index (GCI) methodology of Roache (1994), which proposes the construction of three grids with control area size ratios greater than 1.3. Therefore, three grids, 1, 2, and 3, were built with 3600, 7504, and 14400 hexahedral volumes, respectively.

The grid convergence analysis considered the number average and the mass average molar masses on line A at the steady state. This analysis was performed for both methods (FPQM and DQMoM), using several values of N and n. The methodology described in the next section determined the required variables on line A.

4.5. Post-processing data

The numerical results of DQMoM and FPQM were compared using different response variables:

- the molar mass profiles on line A at $t = 1.5$ s, when the steady-state is reached at this line,
- the transient bulk molar mass profiles at the output,
- the two-dimensional contour plot of the molar masses,
- the yield curve of some common oil fractions at the output, and
- the computational costs.

The molar mass profile on line A was obtained using the *sampleDict* tool, which can sample field data on a 1D line using different interpolation types. We applied the linear weighted interpolation using cell values, with one hundred points evenly spaced along line A.

The bulk values of the variables of interest, $\overline{\varphi}$, were obtained through their integration at the outlet boundary, as follows:

$$\overline{\varphi} = \frac{\sum_{i=1}^{e} \phi_i \left(\varphi_f\right)_i}{\sum_{i=1}^{e} \phi_i} \tag{42}$$

where f represents the interpolated value of the variable at the center of face i that belongs to the outlet surface, and ϕ_i is the mass flow rate across this face, given by $\phi = \mathbf{S} \cdot (\rho \mathbf{v})_f$.

We lumped the products of the cracking reaction into five common oil fractions: liquefied petroleum gas (LPG), gasoline, kerosene, light gas oil (LGO), and heavy gas oil (HGO), in order to give a practical sense to the yield curves resulting from the second test case.

We built the yield curves using the bulk values of the variables at the outlet boundary, obtained using Eq. (42). For DQMoM, the distribution was reconstructed from its moments using the Fourier series expansion method (Lage, 2007), as done by Rocha and Lage (2020). Appendix C gives the details of the reconstruction procedure.

5. Results and discussion

5.1. Accuracy of the numerical methods

Figs. 2 and 3 compare the number and mass-average molar masses obtained analytically and using the FPQM and DQMoM, respectively, for test case 1. The value adopted for the kinetic rate ($\sigma = 0.175$) was large enough to promote a relevant variation in the molar mass, reaching approximately 70 % in M_n and 33 % in M_w.

Due to the calculation of λ_{-1}, both numerical methods are more accurate in representing the M_w than the M_n. Moreover, this case shows that the DQMoM is highly accurate for calculating the zeroth and first-order moments. Therefore, the curves of M_w are overlapped in Fig. 3(b).

Fig. 3(a) shows that the increase in the number of quadrature points (N) improves the accuracy of the number-average molar mass obtained by DQMoM. On the other hand, Fig. 2(a) shows that the FPQM results for different n values do not agree with each other and with the analytical solution, indicating that significant errors do exist.

This case also proved the effectiveness of the methodology developed to initialize the FPQM, described in Section 3.2, since Fig. 2 shows that the FPQM initial values of M_w and M_n agree well with the imposed initial conditions.

5.2. Grid convergence analysis

We analyzed the grid convergence on line A at $t = 1.5$ s, where large concentration gradients exist. Figs. 4 and 5 show the grid convergence results for M_n and M_w, obtained by using FPQM and DQMoM, respectively. The profiles of M_n and M_w for grids 2 (7054 volumes) and 3 (14400 volumes) are quite similar. There-

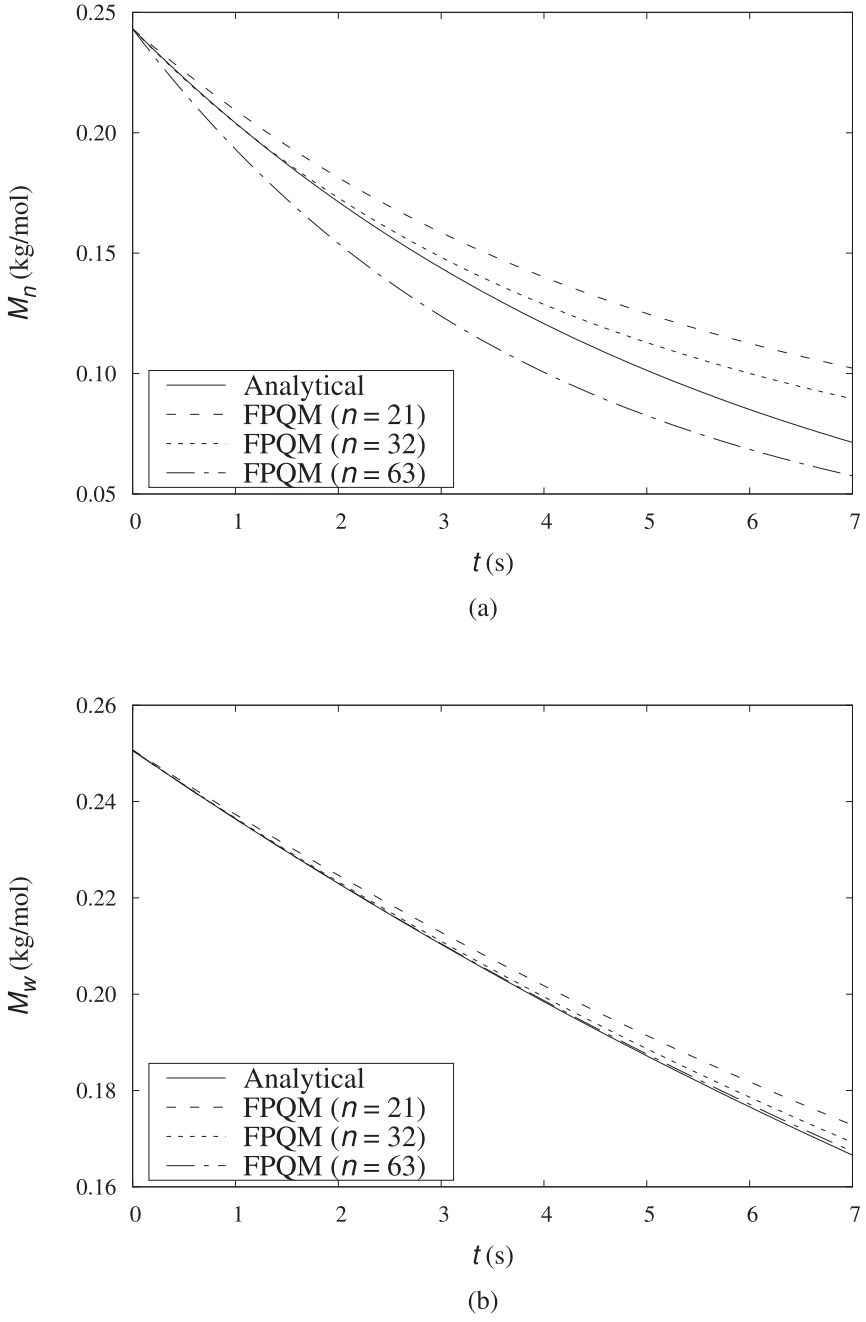

Fig. 2. Accuracy analysis for the FPQM results for the (a) number-average and (b) mass-average molar masses using test case 1 with $n = 21, 32$ and 63.

fore, we assumed that mesh convergence exists for both numerical methods at grid 2.

The value of the average uncertainties calculated by the GCI, from the FPQM results, on line A, at $t = 5s$, were: $\gamma_{M_n} = 3 \times 10^{-4}$ kg/mol and $\gamma_{M_w} = 5 \times 10^{-4}$ kg/mol. The same calculations performed from the DQMoM results generated similar values: $\gamma_{M_n} = 3 \times 10^{-4}$ kg/mol and $\gamma_{M_w} = 4 \times 10^{-4}$ kg/mol. These values are below 0.5% of the values of M_n and M_w, indicating that the simulated results have high reliability.

It is important to mention that although the Figs. 4 and 5 only present the results of DQMoM with $N = 5$ and FPQM with $n = 32$, the same analysis was carried out using the other values of N (3, 4 and 6) and n (21 and 63). All these cases showed a similar convergence pattern.

5.3. Result comparison between DQMoM and FPQM

Fig. 6 and 7 shows the DQMoM convergence for varying N values and the effect of the number of discretization intervals, n, in the FPQM solution for test case 2 using results for the number-average and mass-average molar masses. While Fig. 6 shows these values at $t = 1.5$ s on line A, Fig. 7 presents their bulk values at the outlet for the whole simulations. Both figures show the excellent convergence behavior of DQMoM, especially for M_w. On the other hand, the FPQM solutions with the reduced number of discretization intervals ($n = 21$ and 32), as given by the procedure explained in Appendix B, largely disagree with the FPQM solution with $n = 63$. Besides, the FPQM solution with $n = 32$ is closer to the DQMoM converged results than its solution with $n = 21$ or 63, which indicates that FPQM accumulates enough numerical error

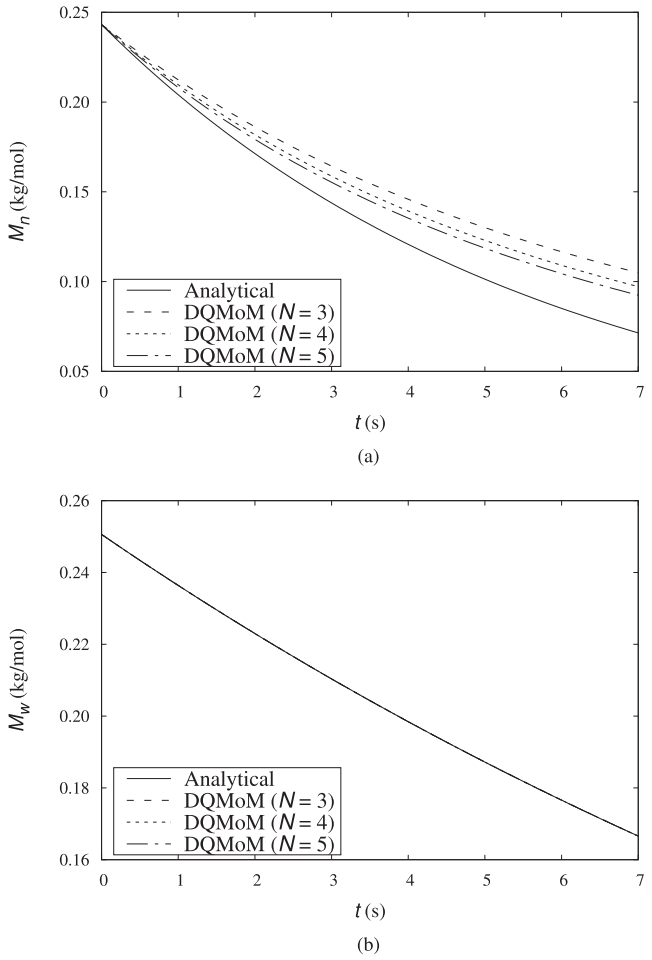

Fig. 3. Accuracy analysis for the DQMoM results for the (a) number-average and (b) mass-average molar masses using test case 1 and $N = 3, 4$ and 5. It should be noted that all curves overlap in (b).

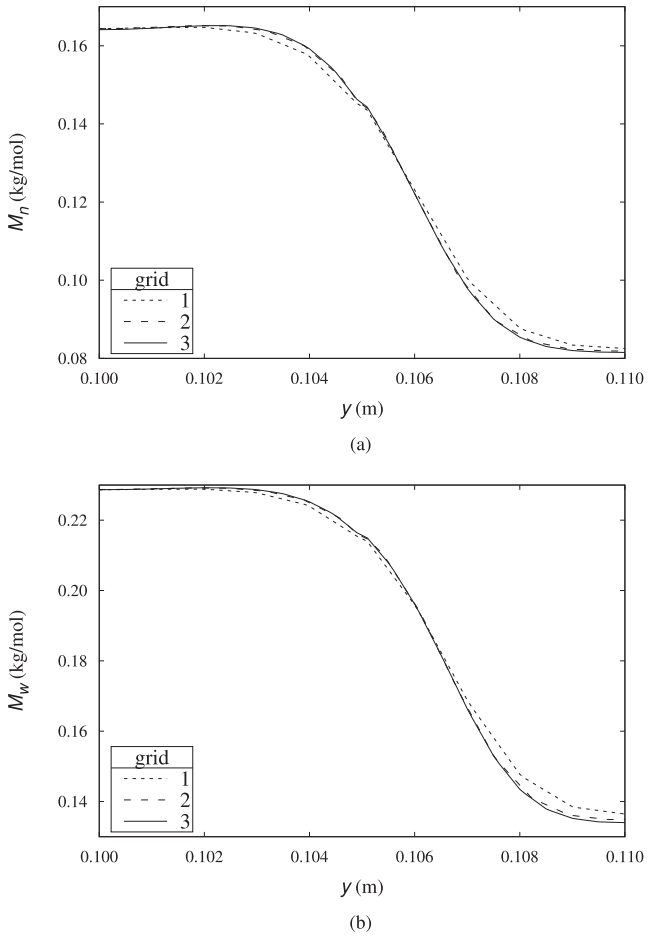

Fig. 4. Mesh convergence analysis of FPQM with $n = 32$ for test case 2: results at $t = 1.5$ s on line A for the (a) number-average and (b) mass-average molar masses.

to render the solution incorrect for the original number of pseudo-components in the inlet discrete distribution. Therefore, in the following, the FPQM solution with the reduced number of intervals, $n = 32$, is compared to the DQMoM results.

Fig. 8 compares the contour plots of M_n fields at $t = 1.5$ s obtained using the DQMoM with $N = 5$ and the FPQM with $n = 32$. Even though the solutions are close, there noticeable differences near inlet 1. Since the DQMoM solution is converged, the FPQM solution presents noticeable numerical errors.

Fig. 9 shows the hydrocarbon mixture's steady-state cumulative mass fraction distribution at both inlets and outlet using the results for the FPQM ($n = 32$) and DQMoM ($N = 5$) simulations. This figure also shows the I-ranges of usual petroleum lumps. Table 2 presents the mass fractions of these petroleum lumps for the simulations using FPQM and DQMoM. While the lump mass fractions for the DQMoM results with all N values agree within 0.85%, the agreement between the FPQM results and the converged DQMoM results is considerably worse. Thus, the DQMoM results with $N = 3$ are more accurate than any FPQM simulation results.

Table 3 shows the computational costs of the simulations of test case 2 using the FPQM and DQMoM for varying N and n values. The DQMoM solution is always faster. Comparing the DQMoM with $N = 3$ and FPQM with $n = 63$, both using the original discrete distributions, with the former more accurate than the latter, the speedup is 4.86.

6. Conclusions

This work implemented two methodologies to simulate semi-continuous reactive mixtures' flow in OpenFOAM®. The first is a fixed point discretization method (FPQM) previously developed for zeroth-dimensional models and continuous mass fraction distributions. We extended it to field problems and discrete distributions as initial and inlet data. The other method is the DQMoM application to solve flows of semi-continuous mixtures that we extended to reactive flows.

The DQMoM was accurate and led to converged solutions both regarding meshes and numbers of quadrature points. The FPQM could not obtain the same accuracy for discrete concentration distributions inlet data, probably due to the accumulation of numerical errors. Besides, DQMOM was up to 4.9 faster than FPQM for our reactive flow test case.

Therefore, the results show that DQMoM is superior to FPQM in simulating semi-continuous reactive mixtures' flows.

Declaration of Competing Interest

The authors declare that they have no known competing financial interests or personal relationships that could have appeared to influence the work reported in this paper.

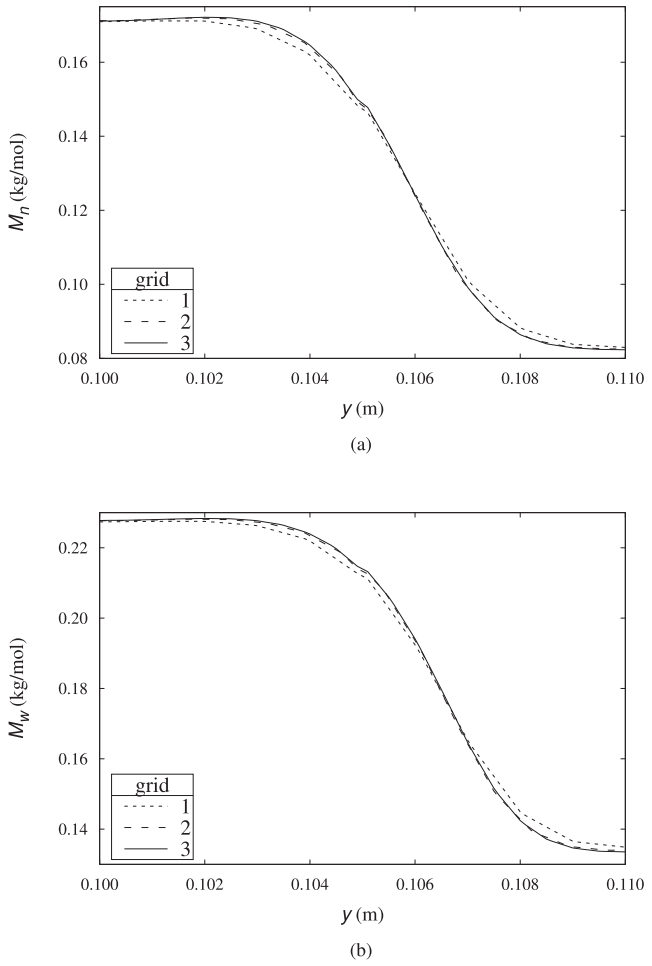

Fig. 5. Mesh convergence analysis of DQMoM with $N = 5$ for test case 2: results at $t = 1.5$ s on line A for the (a) number-average and (b) mass-average molar masses.

Acknowledgments

Paulo L. C. Lage acknowledges the financial support from CNPq, Grant Nos. 305276/2019–0 and 305265/2015–6.

Appendix A. DQMoM equations for the reactive flow of a continuous component

As mentioned earlier in Section 3.1, the DQMoM application generates a system of differential equations. It consists of three steps: (i) the replacement of f by its discrete form given by Eq. (6) in the mass conservation equation for the continuous component, Eq. (4), ii) the application of the moment operator (Eq. 7) to the resulting equation, and (iii) the usage of the following property:

$$\int_{I_{min}}^{I_{max}} \varphi(I)\delta^{(n)}(I-I_i)dI = (-1)^n\varphi^{(n)}(I_i), \quad n \geqslant 0 \tag{A.1}$$

for any function φ and $I_i \in (I_{min}, I_{max})$, where (n) indicates the n-order derivative in respect to I.

For clarity, we describe this procedure for each term of Eq. (6), using Cartesian index notation with the sum convention.

A.1. Accumulation Term

$$\begin{aligned}\frac{\partial f}{\partial t} &= \frac{\partial}{\partial t}\left[\sum_{i=1}^{N}\omega_i\delta(I-I_i)\right] \\ &= \sum_{i=1}^{N}\frac{\partial\omega_i}{\partial t}\delta(I-I_i) - \sum_{i=1}^{N}\omega_i\frac{\partial I_i}{\partial t}\delta\prime(I-I_i)\end{aligned} \tag{A.2}$$

and

$$\begin{aligned}\int_{I_{min}}^{I_{max}} I^k\frac{\partial f}{\partial t}dI = &\sum_{i=1}^{N}\frac{\partial\omega_i}{\partial t}\int_{I_{min}}^{I_{max}} I^k\delta(I-I_i)dI \\ &-\sum_{i=1}^{N}\omega_i\frac{\partial I_i}{\partial t}\int_{I_{min}}^{I_{max}} I^k\delta\prime(I-I_i)dI \\ = &\sum_{i=1}^{N}\frac{\partial\omega_i}{\partial t}I_i^k + \sum_{i=1}^{N}\omega_i\frac{\partial I_i}{\partial t}kI_i^{k-1}\end{aligned} \tag{A.3}$$

A.2. Advective Term

$$\begin{aligned}\nabla\cdot(f\mathbf{v}) &= \tfrac{\partial[f(I,t)v_n]}{\partial x_n} = \tfrac{\partial}{\partial x_n}\left\{\left[\sum_{i=1}^{N}\omega_i\delta(I-I_i)\right]v_n\right\} \\ &= \sum_{i=1}^{N}\tfrac{\partial(\omega_i v_n)}{\partial x_n}\delta(I-I_i) - \sum_{i=1}^{N}\omega_i v_n\tfrac{\partial I_i}{\partial x_n}\delta\prime(I-I_i)\end{aligned} \tag{A.4}$$

and

$$\begin{aligned}\int_{I_{min}}^{I_{max}} I^k\nabla\cdot(f\mathbf{v})dI = &\sum_{i=1}^{N}\tfrac{\partial(\omega_i v_n)}{\partial x_n}\int_{I_{min}}^{I_{max}} I^k\delta(I-I_i)dI \\ &-\sum_{i=1}^{N}\omega_i v_n\tfrac{\partial I_i}{\partial x_n}\int_{I_{min}}^{I_{max}} I^k\delta\prime(I-I_i)dI \\ = &\sum_{i=1}^{N}\tfrac{\partial(\omega_i v_n)}{\partial x_n}I_i^k + \sum_{i=1}^{N}\omega_i v_n\tfrac{\partial I_i}{\partial x_n}kI_i^{k-1} \\ = &\sum_{i=1}^{N}\tfrac{\partial(\omega_i v_n)}{\partial x_n}I_i^k + \sum_{i=1}^{N}\omega_i\tfrac{\partial(I_i v_n)}{\partial x_n}kI_i^{k-1} - \sum_{i=1}^{N}\omega_i I_i\tfrac{\partial v_n}{\partial x_n}kI_i^{k-1}\end{aligned} \tag{A.5}$$

A.3. Diffusive Term

$$\begin{aligned}\nabla\cdot[D(I)\nabla f] = &\tfrac{\partial}{\partial x_n}\left[D(I)\tfrac{\partial f}{\partial x_n}\right] = \tfrac{\partial}{\partial x_n}\left\{D(I)\tfrac{\partial}{\partial x_n}\left[\sum_{i=1}^{N}\omega_i\delta(I-I_i)\right]\right\} \\ = &\sum_{i=1}^{N}\tfrac{\partial}{\partial x_n}\left[D(I)\tfrac{\partial\omega_i}{\partial x_n}\delta(I-I_i)\right] - \sum_{i=1}^{N}\tfrac{\partial}{\partial x_n}\left[D(I)\omega_i\tfrac{\partial I_i}{\partial x_n}\delta\prime(I-I_i)\right] \\ = &\sum_{i=1}^{N}\tfrac{\partial}{\partial x_n}\left(D(I)\tfrac{\partial\omega_i}{\partial x_n}\right)\delta(I-I_i) - \sum_{i=1}^{N}D(I)\tfrac{\partial\omega_i}{\partial x_n}\tfrac{\partial I_i}{\partial x_n}\delta\prime(I-I_i) \\ &-\sum_{i=1}^{N}\tfrac{\partial}{\partial x_n}\left(D(I)\omega_i\tfrac{\partial I_i}{\partial x_n}\right)\delta\prime(I-I_i) + \sum_{i=1}^{N}D(I)\omega_i\tfrac{\partial I_i}{\partial x_n}\tfrac{\partial I_i}{\partial x_n}\delta\prime\prime(I-I_i)\end{aligned} \tag{A.6}$$

and

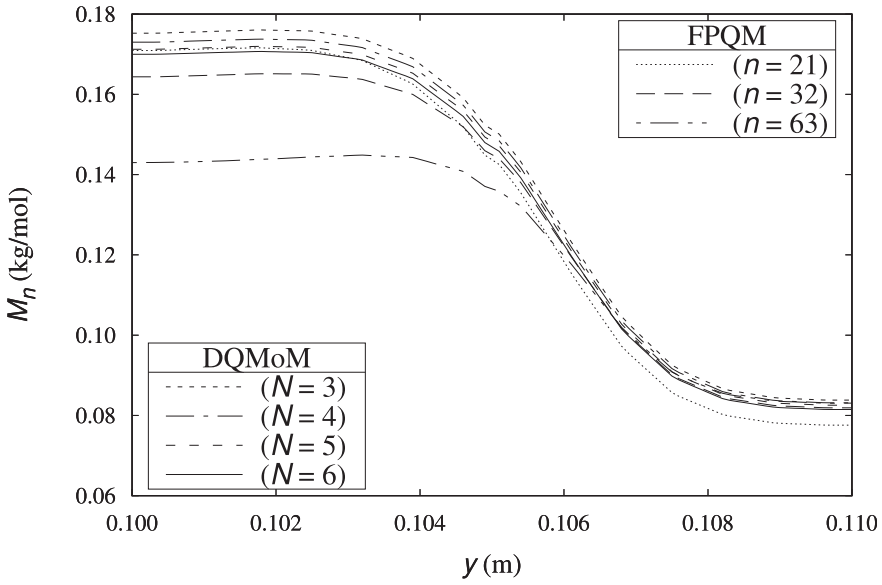

(a)

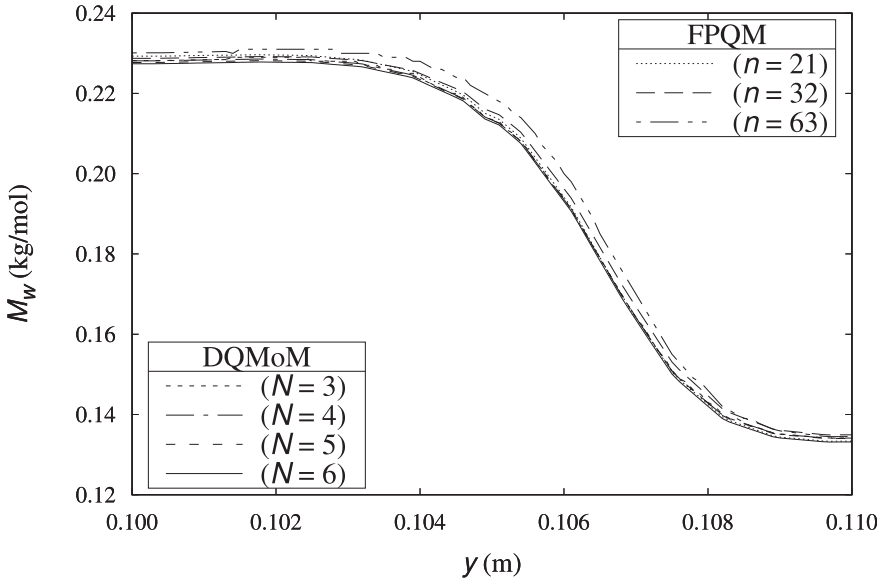

(b)

Fig. 6. DQMoM and FPQM convergence analyses for test case 2: results at $t = 1.5$ s on line A for the (a) number-average and (b) mass-average molar masses.

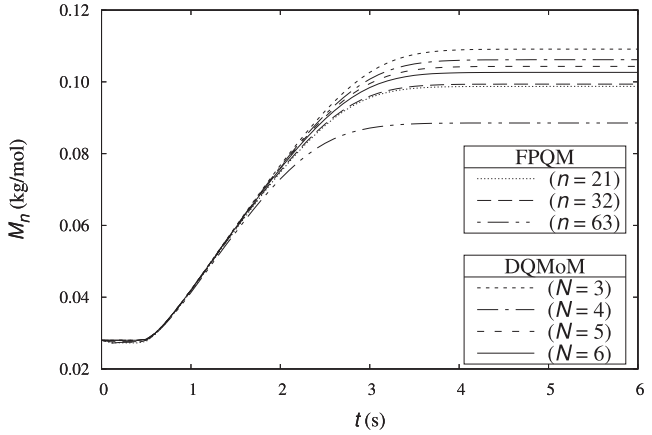

(a)

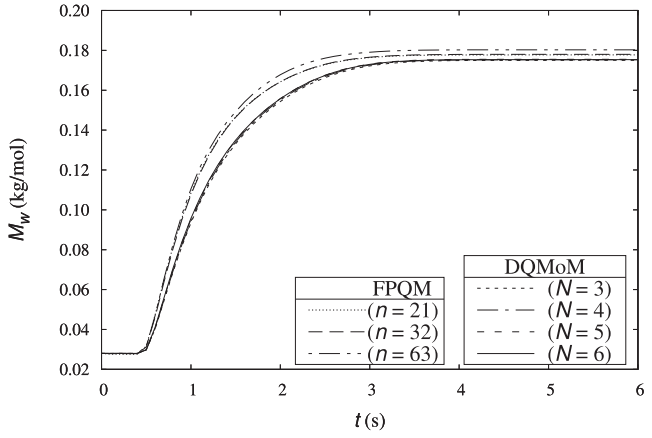

(b)

Fig. 7. DQMoM and FPQM convergence analyses for test case 2: results for the time evolution of the bulk (a) number-average and (b) mass-average molar masses at the outlet.

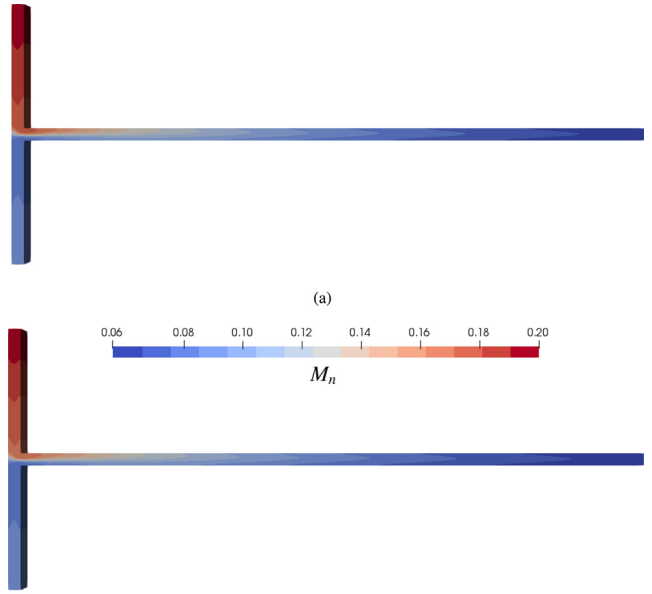

(a)

(b)

Fig. 8. Contour plots of the number-average molar mass results for test case 2 at $t = 1.5$ s obtained using (a) DQMoM ($N = 5$) and (b) FPQM ($n = 32$).

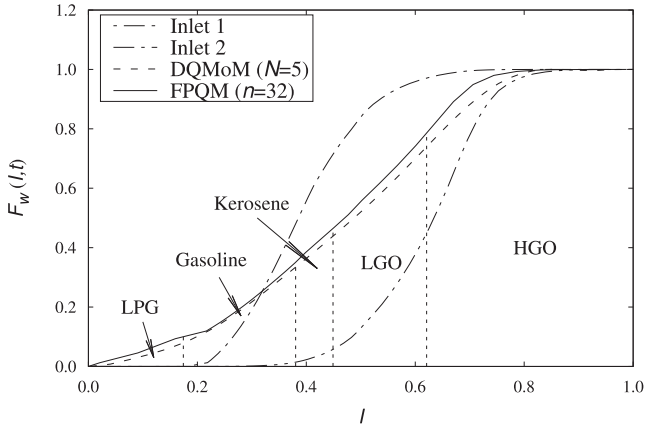

Fig. 9. Steady-state cumulative mass fraction distribution at the two inlets and the outlet for test case 2 obtained using FPQM ($n = 32$) and DQMoM ($N = 5$).

$$
\begin{aligned}
\int_{I_{min}}^{I_{max}} I^k \nabla\cdot[D(I)\nabla f]dI = & \sum_{i=1}^{N}\int_{I_{min}}^{I_{max}} I^k \tfrac{\partial}{\partial x_n}\left(D(I)\tfrac{\partial \omega_i}{\partial x_n}\right)\delta(I-I_i)dI \\
& - \sum_{i=1}^{N}\tfrac{\partial \omega_i}{\partial x_n}\tfrac{\partial I_i}{\partial x_n}\int_{I_{min}}^{I_{max}} I^k D(I)\delta\prime(I-I_i)dI \\
& - \sum_{i=1}^{N}\int_{I_{min}}^{I_{max}} I^k \tfrac{\partial}{\partial x_n}\left(D(I)\omega_i\tfrac{\partial I_i}{\partial x_n}\right)\delta\prime(I-I_i)dI \\
& + \sum_{i=1}^{N}\omega_i\tfrac{\partial I_i}{\partial x_n}\tfrac{\partial I_i}{\partial x_n}\int_{I_{min}}^{I_{max}} I^k D(I)\delta\prime\prime(I-I_i)dI \\
= & \sum_{i=1}^{N}\tfrac{\partial}{\partial x_n}\left(D(I_i)\tfrac{\partial \omega_i}{\partial x_n}\right)I_i^k \\
& + \sum_{i=1}^{N}\tfrac{\partial \omega_i}{\partial x_n}\tfrac{\partial I_i}{\partial x_n}D(I_i)kI_i^{k-1} + \sum_{i=1}^{N}\tfrac{\partial \omega_i}{\partial x_n}\tfrac{\partial I_i}{\partial x_n}D\prime(I_i)I_i^k \\
& + \sum_{i=1}^{N}\tfrac{\partial}{\partial x_n}\left(D(I_i)\omega_i\tfrac{\partial I_i}{\partial x_n}\right)kI_i^{k-1} + \sum_{i=1}^{N}\tfrac{\partial}{\partial x_n}\left(D\prime(I_i)\omega_i\tfrac{\partial I_i}{\partial x_n}\right)I_i^k \\
& + \sum_{i=1}^{N}\omega_i\tfrac{\partial I_i}{\partial x_n}\tfrac{\partial I_i}{\partial x_n}\left[k(k-1)I_i^{k-2}D(I_i) + 2kI_i^{k-1}D\prime(I_i) + I_i^k D\prime\prime(I_i)\right],
\end{aligned}
\tag{A.7}
$$

which can be further manipulated to give:

$$
\begin{aligned}
\int_{I_{min}}^{I_{max}} I^k \nabla\cdot[D(I)\nabla f]dI = & \sum_{i=1}^{N}\tfrac{\partial}{\partial x_n}\left(D(I_i)\tfrac{\partial \omega_i}{\partial x_n}\right)I_i^k + \sum_{i=1}^{N}\tfrac{\partial}{\partial x_n}\left(D(I_i)\tfrac{\partial I_i}{\partial x_n}\right)\omega_i kI_i^{k-1} \\
& + \sum_{i=1}^{N}2\tfrac{\partial \omega_i}{\partial x_n}\tfrac{\partial I_i}{\partial x_n}D(I_i)kI_i^{k-1} + \sum_{i=1}^{N}2\tfrac{\partial \omega_i}{\partial x_n}\tfrac{\partial I_i}{\partial x_n}D\prime(I_i)I_i^k \\
& + \sum_{i=1}^{N}\tfrac{\partial}{\partial x_n}\left(D\prime(I_i)\tfrac{\partial I_i}{\partial x_n}\right)\omega_i I_i^k \\
& + \sum_{i=1}^{N}\omega_i\tfrac{\partial I_i}{\partial x_n}\tfrac{\partial I_i}{\partial x_n}\left[k(k-1)I_i^{k-2}D(I_i) + 2kI_i^{k-1}D\prime(I_i) + I_i^k)D\prime\prime(I_i)\right]
\end{aligned}
\tag{A.8}
$$

A.4. Compressibility Term

$$
\begin{aligned}
\nabla\cdot\left[D(I)f\tfrac{\nabla\rho}{\rho}\right] = & \tfrac{\partial}{\partial x_n}\left[D(I)f\tfrac{1}{\rho}\tfrac{\partial\rho}{\partial x_n}\right] = \tfrac{\partial}{\partial x_n}\left\{D(I)\left[\sum_{i=1}^{N}\omega_i\delta(I-I_i)\right]\tfrac{1}{\rho}\tfrac{\partial\rho}{\partial x_n}\right\} \\
= & \sum_{i=1}^{N}\tfrac{\partial}{\partial x_n}\left(\omega_i D(I)\tfrac{1}{\rho}\tfrac{\partial\rho}{\partial x_n}\right)\delta(I-I_i) \\
& - \sum_{i=1}^{N}\omega_i D(I)\tfrac{1}{\rho}\tfrac{\partial\rho}{\partial x_n}\tfrac{\partial I_i}{\partial x_n}\delta\prime(I-I_i)
\end{aligned}
\tag{A.9}
$$

Table 2
Steady-state mass fractions of the petroleum lumps at the outlet obtained using FPQM and DQMoM ($s = 2N - 1$).

Mass fraction	DQMoM (N)[1]				FPQM (n)		
[%]	3	4	5	6	21	32	63
LPG	8.13	8.61	8.23	8.76	10.81	10.02	8.32
Gasoline	26.28	25.63	26.62	26.38	25.06	25.05	23.27
Kerosene	12.46	11.48	10.77	10.78	11.75	11.42	10.69
LGO	31.22	31.72	31.28	30.78	32.80	32.11	30.30
HGO	21.91	22.55	23.10	23.30	19.58	21.40	27.42
Mean difference[2]	0.85	0.66	0.30	–	2.02	1.29	1.65

[1] using $s = 2N - 1$ in the distribution reconstruction
[2] arithmetic mean of the absolute differences using DQMoM with $N = 6$ as reference

Table 3
CPU times for test case 2 simulations up to $t = 7$ s on grid 2.

	DQMoM (N)				FPQM (n)		
	3	4	5	6	21	32	63
CPU time [h]	70.52	88.13	101.98	122.72	105.53	178.68	342.82

and

$$\begin{aligned}\int_{I_{min}}^{I_{max}} I^k \nabla\cdot\left[D(I)f\tfrac{\nabla\rho}{\rho}\right]dI = &\sum_{i=1}^{N}\int_{I_{min}}^{I_{max}} I^k \tfrac{\partial}{\partial x_n}\left(\omega_i D(I)\tfrac{1}{\rho}\tfrac{\partial\rho}{\partial x_n}\right)\delta(I-I_i)dI\\ &-\sum_{i=1}^{N}\omega_i\tfrac{1}{\rho}\tfrac{\partial\rho}{\partial x_n}\tfrac{\partial l_i}{\partial x_n}\int_{I_{min}}^{I_{max}} I^k D(I)\delta\prime(I-I_i)dI\\ =&\sum_{i=1}^{N}\tfrac{\partial}{\partial x_n}\left(\omega_i D(I_i)\tfrac{1}{\rho}\tfrac{\partial\rho}{\partial x_n}\right)I_i^k\\ &+\sum_{i=1}^{N}\omega_i\tfrac{1}{\rho}\tfrac{\partial\rho}{\partial x_n}\tfrac{\partial l_i}{\partial x_n}D(I_i)kI_i^{k-1}\\ &+\sum_{i=1}^{N}\omega_i\tfrac{1}{\rho}\tfrac{\partial\rho}{\partial x_n}\tfrac{\partial l_i}{\partial x_n}D\prime(I_i)I_i^k\\ =&\sum_{i=1}^{N}\tfrac{\partial}{\partial x_n}\left(\omega_i D(I_i)\tfrac{1}{\rho}\tfrac{\partial\rho}{\partial x_n}\right)I_i^k\\ &+\sum_{i=1}^{N}\omega_i\tfrac{\partial}{\partial x_n}\left(I_i D(I_i)\tfrac{1}{\rho}\tfrac{\partial\rho}{\partial x_n}\right)kI_i^{k-1}\\ &-\sum_{i=1}^{N}\omega_i I_i\tfrac{\partial}{\partial x_n}\left(D(I_i)\tfrac{1}{\rho}\tfrac{\partial\rho}{\partial x_n}\right)kI_i^{k-1}\\ &+\sum_{i=1}^{N}\omega_i\tfrac{1}{\rho}\tfrac{\partial\rho}{\partial x_n}\tfrac{\partial l_i}{\partial x_n}D\prime(I_i)I_i^k\end{aligned}\tag{A.10}$$

A.5. Reaction Term

$$\begin{aligned}r(I) = &-b_f(I)f(I,t)+\int_I^{I_{max}} v(I\prime)b_f(I\prime)\Omega(I,I\prime)f(I\prime,t)dI\prime\\ =&-b_f(I)\left[\sum_{i=1}^{N}\omega_i\delta(I-I_i)\right]+\int_I^{I_{max}} v(I\prime)b_f(I\prime)\Omega(I,I\prime)\\ &\left[\sum_{i=1}^{N}\omega_i\delta(I\prime-I_i)\right]dI\prime\end{aligned}\tag{A.11}$$

and

$$\begin{aligned}\int_{I_{min}}^{I_{max}} I^k r(I)dI = &-\int_{I_{min}}^{I_{max}} b_f(I)I^k\left[\sum_{i=1}^{N}\omega_i\delta(I-I_i)\right]dI\\ &+\int_{I_{min}}^{I_{max}} I^k\int_I^{I_{max}} v(I\prime)b_f(I\prime)\Omega(I,I\prime)\left[\sum_{i=1}^{N}\omega_i\delta(I\prime-I_i)\right]dI\prime dI\\ =&-\sum_{i=1}^{N}\omega_i\int_{I_{min}}^{I_{max}} b_f(I)I^k\delta(I-I_i)dI\\ &+\sum_{i=1}^{N}\omega_i\int_{I_{min}}^{I_{max}} v(I\prime)b_f(I\prime)\delta(I\prime-I_i)\left(\int_{I_{min}}^{I\prime} I^k\Omega(I,I\prime)dI\right)dI\prime\\ =&-\sum_{i=1}^{N}\omega_i b_f(I_i)I_i^k+\sum_{i=1}^{N}\omega_i v(I_i)b_f(I_i)L_k(I_i)\end{aligned}\tag{A.12}$$

where $L_k(I)$ is defined in Eq. (14).

A.6. DQMoM equations

Gathering all the results given above, we can write the dyadic form of the DQMoM equations as

$$\begin{aligned}&\sum_{i=1}^{N}\tfrac{\partial\omega_i}{\partial t}I_i^k+\sum_{i=1}^{N}\omega_i\tfrac{\partial l_i}{\partial t}kI_i^{k-1}\\ &+\sum_{i=1}^{N}\nabla\cdot(\omega_i\mathbf{v})I_i^k+\sum_{i=1}^{N}\omega_i\nabla\cdot(I_i\mathbf{v})kI_i^{k-1}-\sum_{i=1}^{N}\omega_i I_i(\nabla\cdot\mathbf{v})kI_i^{k-1}\\ &-\sum_{i=1}^{N}\nabla\cdot(D(I_i)\nabla\omega_i)I_i^k-\sum_{i=1}^{N}\nabla\cdot(D(I_i)\nabla I_i)\omega_i kI_i^{k-1}\\ &-\sum_{i=1}^{N}2\nabla\omega_i\cdot\nabla I_i D(I_i)kI_i^{k-1}\\ &-\sum_{i=1}^{N}2\nabla\omega_i\cdot\nabla I_i D\prime(I_i)I_i^k-\sum_{i=1}^{N}\nabla\cdot(D\prime(I_i)\nabla I_i)\omega_i I_i^k\\ &-\sum_{i=1}^{N}\omega_i\nabla I_i\cdot\nabla I_i\left[k(k-1)I_i^{k-2}D(I_i)+2kI_i^{k-1}D\prime(I_i)+I_i^k D\prime\prime(I_i)\right]\\ &+\sum_{i=1}^{N}\nabla\cdot\left(\omega_i D(I_i)\tfrac{\nabla\rho}{\rho}\right)I_i^k+\sum_{i=1}^{N}\nabla\cdot\left(I_i D(I_i)\tfrac{\nabla\rho}{\rho}\right)\omega_i kI_i^{k-1}\\ &-\sum_{i=1}^{N}\nabla\cdot\left(D(I_i)\tfrac{\nabla\rho}{\rho}\right)\omega_i I_i kI_i^{k-1}+\sum_{i=1}^{N}\omega_i\tfrac{\nabla\rho}{\rho}\cdot\nabla I_i D\prime(I_i)I_i^k\\ &+\sum_{i=1}^{N}\omega_i b_f(I_i)I_i^k-\sum_{i=1}^{N}\omega_i v(I_i)b_f(I_i)L_k(I_i)=0,\quad k=0,1,\ldots,\end{aligned}\tag{A.13}$$

which can be rewritten in the form given by Eqs. (8)–(14).

Appendix B. The initialization of FPQM with a discrete initial distribution

As mentioned in Section 3.2, the FPQM solution needs an alternate method when the initial or the inlet concentration distribution is discrete with q lumps, as given by Eq. (19). It can be summarized in the following sequential steps:

1. Choose the number of discrete pseudo-components, $m = 1, 2$ or 3, which must belong to each partition interval (I_i, I_{i+1}).
2. Define the number of partition intervals: $n = (q + \eta)/m$ where η is the smallest positive integer that allows an exact division by m. If $\eta > 0$, add η pseudo-components with zero mass concentration after J_q.
3. Calculate the mass concentration in each interval by

$$\rho_i(0) = \begin{cases} \tilde{\rho}_i, & \text{for } m = 1 \\ \tilde{\rho}_{2i-1} + \tilde{\rho}_{2i}, & \text{for } m = 2, \quad i = 1, \ldots, n, \\ \tilde{\rho}_{3i-2} + \tilde{\rho}_{3i-1} + \tilde{\rho}_{3i}, & \text{for } m = 3 \end{cases} \tag{A.14}$$

4. Assume that $I_0 = 0$ and place the remaining nodal points (I_i) accordingly to:

$$I_i = \frac{J_{mi} + J_{mi+1}}{2}, \quad i = 1, \ldots, n-1 \tag{A.15}$$

$$I_n = J_n + \left(J_{n-(m-1)} - I_{n-1}\right) \tag{A.16}$$

5. Calculate G_i and H_i for $i = 0, \ldots, n-1$ from their definition (Eq. 18).
6. Assume $f(I_n, 0) = 0$ and from the heaviest to the lightest pseudo-component, calculate $f(I_i, 0)$ by:

$$f(I_i, 0) = \frac{1}{G_i}[\rho_i(0) - f(I_{i+1}, 0)H_i], \quad i = n-1, \ldots, 1 \tag{A.17}$$

For the discrete distribution given by Table 1, $q = 63$ and, therefore, $n = 63$, 32 and 21 for $m = 1$, 2 and 3, respectively.

Appendix C. Reconstruction of the distribution function

The mass concentration distribution function, f, was reconstructed using the Fourier series expansion method given by Lage (2007), which represents the function as a truncate series using an orthonormal polynomial basis. For Legendre polynomials, we have:

$$f(I) \simeq \sum_{j=0}^{s} \Phi_j \ell_j(I), \quad I \in [0, 1] \tag{A.18}$$

where ℓ_j are the shifted Legendre polynomials defined in the interval, $[0, 1]$, and Φ_j is the Fourier coefficient, defined by:

$$\Phi_j = \int_0^1 f(I)\ell_j(I)dI \tag{A.19}$$

which can be calculated by using the quadrature rule defined by:

$$\int_0^1 \varphi(I)f(I)dI \cong \sum_{i=1}^{N} \omega_i \varphi(I_i) \tag{A.20}$$

where φ is any function.

The Eq. (A.19) can be calculated exactly, $\forall j \leqslant 2N - 1$, leading to:

$$\Phi_j = \sum_{i=1}^{N} \omega_i \ell_j(I_i) \tag{A.21}$$

Therefore, a natural choice is $s = 2N - 1$.

The cumulative mass fraction distribution was calculated from:

$$F_w(I_i) = \int_0^{I_i} f(I)dI \tag{A.22}$$

using the AUTOQUAD package (Lage and Rangel, 1993) to perform the numerical integration.

As done by Rocha and Lage (2020), we calculated the Legendre polynomials from the three-term recurrence relation, whose coefficients were computed using the ORTHPOL package (Gautschi, 1994).

References

Buffo, A., Vanni, M., Marchisio, D.L., Fox, R.O., 2013. Multivariate quadrature-based moments methods for turbulent polydisperse gas–liquid systems. Int. J. Multiphase Flow 50, 41–57.

Chicralla, F.C., Lage, P.L.C., Secchi, A.R., 2019. Quadrature algorithms for phase equilibrium of continuous mixtures. Brazil. J. Chem. Eng. 36, 1303–1318.

Cooney, A., Singer, S., 2018. Modeling multicomponent fuel droplet vaporization with finite liquid diffusivity using coupled algebraic-dqmom with delumping. Fuel 212, 554–565. https://doi.org/10.1016/j.fuel.2017.10.056.

Elizalde, I., Rodríguez, M.A., Ancheyta, J., 2009. Application of continuous kinetic lumping modeling to moderate hydrocracking of heavy oil. Appl. Catal. A: General 365, 237–242. https://doi.org/10.1016/j.apcata.2009.06.018.

Favero, J.L., Ferreira, G.G.S., Silva, L.F.L.R., Lage, P.L.C., 2016. Solving numerical stability problems in multiphase flows with large interphase heat transfer. In: 11th OpenFOAM Workshop. Guimarães, Portugal, pp. 194–195.

Gaskell, P., Lau, A., 1988. Curvature-compensated convective transport: Smart, a new boundedness-preserving transport algorithm. Int. J. Numer. Methods Fluids 8, 617–641. https://doi.org/10.1002/fld.1650080602.

Gautschi, W., 1994. Algorithm 726: Orthpol–a package of routines for generating orthogonal polynomials and gauss-type quadrature rules. ACM Trans. Math. Softw. 20, 21–62. https://doi.org/10.1145/174603.174605.

Govindhakannan, J., Riggs, J.B., 2007. On the construction of a continuous concentration-reactivity function for the continuum lumping approach. Industr. Eng. Chem. Res. 46, 1653–1656. https://doi.org/10.1021/ie0607191.

Harten, A., 1983. High resolution schemes for hyperbolic conservation laws. J. Comput. Phys. 49, 357–393. https://doi.org/10.1016/0021-9991(83)90136-5.

Jatobá, L.F.C., Lage, P.L.C., Silva, L.F.L.R., 2014. Simulation of the compressible flow with mass transfer of semi-continuous mixtures using the direct quadrature method of moments. Comput. Chem. Eng. 64, 153–166. https://doi.org/10.1016/j.compchemeng.2014.02.011.

Jatobá, L.F.C., 2010. Simulação do escoamento de misturas contínuas usando quadratura adaptativa. Master's thesis. Instituto Alberto Luiz Coimbra de Pós-Graduação e Pesquisa de Engenharia da Universidade Federal do Rio de Janeiro.

Lage, P.L.C., 2007. The quadrature method of moments for continuous thermodynamics. Computers & Chemical Engineering 31, 782–799. https://doi.org/10.1016/j.compchemeng.2006.08.005.

Lage, P.L.C., Rangel, R.H., 1993. Total thermal radiation absorption by a single spherical droplet. Journal of thermophysics and heat transfer 7, 101–109. https://doi.org/10.2514/3.11576.

Laurent, C., Lavergne, G., Villedieu, P., 2009. Continuous thermodynamics for droplet vaporization: Comparison between gamma-pdf model and qmom. Comptes Rendus Mécanique 337, 449–457.

Laurent, F., Nguyen, T.T., 2017. Realizable second-order finite-volume schemes for the advection of moment sets of the particle size distribution. J. Comput. Phys., 309–338

Laxminarasimhan, C.S., Verma, R.P., Ramachandran, P.A., 1996. Continuous lumping model for simulation of hydrocracking. AIChE J. 42, 2645–2653. https://doi.org/10.1002/aic.690420925.

Leonard, B.P., 1988. Simple high-accuracy resolution program for convective modelling of discontinuities. International journal for numerical methods in fluids 8, 1291–1318. https://doi.org/10.1002/fld.1650081013.

Marchisio, D., Fox, R., 2005. Solution of the population balance equation using the direct quadrature method of moments. Journal of Aeorosol Science 36, 43–73.

Mccoy, B.J., 1996. Continuous kinetics of cracking reactions: Thermolysis and pyrolysis. Chem. Eng. Sci. 51, 2903–2908. https://doi.org/10.1016/0009-2509(96)00172-8.

McGraw, R., 1997. Description of aerosol dynamics by the quadrature method of moments. Aerosol Sci. Technol. 27, 255–265.

Nguyen, T.T., Laurent, F., Fox, R.O., Massot, M., 2016. Solution of population balance equations in applications with fine particles: Mathematical modeling and numerical schemes. J. Comput. Phys. 325, 129–156.

Okino, M.S., Mavrovouniotis, M.L., 1998. Simplification of mathematical models of chemical reaction systems. Chemical reviews 98, 391–408.

Passalacqua, A., Laurent, F., Madadi-Kandjani, E., Heylmun, J.C., Fox, R.O., 2018. An open-source quadrature-based population balance solver for openfoam. Chem. Eng. Sci. 176, 306–318.

Petitfrere, M., Nichita, D.V., Montel, F., 2014. Multiphase equilibrium calculations using the semi-continuous thermodynamics of hydrocarbon mixtures. Fluid Phase Equilib. 362, 365–378.

Roache, P.J., 1994. Perspective: A method for uniform reporting of grid refinement studies. J. Fluids Eng. 116, 405–413. https://doi.org/10.1115/1.2910291.

Rocha, D.C., Lage, P.L.C., 2020. The solution of continuous kinetic lumping models using the adaptive characterization method. AIChE J. 66, e16758. https://doi.org/10.1002/aic.16758.

Rodrigues, R.C., Ahón, V.R.R., Lage, P.L.C., 2012. An adaptive characterization scheme for the simulation of multistage separation of continuous mixtures using the quadrature method of moments. Fluid Phase Equilib. 318, 1–12.

Santos, F.P., Lage, P.L.C., Fontes, C.E., 2013. Numerical aspects of direct quadrature-based moment methods for solving the population balance equation. Braz. J. Chem. Eng. 30, 643–656. https://doi.org/10.1590/S0104-66322013000300021.

Singer, S., 2016. Direct quadrature method of moments with delumping for modeling multicomponent droplet vaporization. Int. J. Heat Mass Transf. 103, 940–954. https://doi.org/10.1016/j.ijheatmasstransfer.2016.07.067.

Singer, S., Hayes, M., Cooney, A., 2021. A hybrid droplet vaporization-adaptive surrogate model using an optimized continuous thermodynamics distribution. Fuel 288. https://doi.org/10.1016/j.fuel.2020.119821.

Vergel, J.L.G., Martignoni, W., Ocone, R., Mori, M., 2015. Modelagem cfd de um reator riser-fcc usando o modelo cinetico de lumping continuo. Blucher Chemical Engineering Proceedings 2, 419–428. https://doi.org/10.5151/ENEMP2015-LE-600.

Vikas, V., Wang, Z.J., Passalacqua, A., Fox, R.O., 2011. Realizable high-order finite-volume schemes for quadrature-based moment methods. J. Comput. Phys. 230, 5328–5352.

Weller, H.G., Jasak, H., Tabor, G., 1998. A tensorial approach to computational continuum mechanics using object-oriented techniques. Comput. Phys. 12, 620–631.